Analytical model for elasto-plastic indentation of a hemispherical surface inclusion

G.J.A.M. Eumelen[a,], A.S.J. Suiker[a], E. Bosco[a], N.A. Fleck[b]

[a] *Department of the Built Environment, Eindhoven University of Technology, P.O. Box 513, 5600 MB Eindhoven, The Netherlands*
[b] *Department of Engineering, University of Cambridge, Trumpington Street, Cambridge CB2 1PZ, United Kingdom*

Abstract

An analytical model is developed to deduce the elastic and plastic properties of a hemispherical inclusion embedded in the surface of a semi-infinite solid from its indentation response. The model differs from the approaches presented in the literature by starting from the analytical expressions for the elastic and elasto-plastic indentation responses of homogeneous solids, and adapting them by replacing the modulus of the homogeneous ~~modulu~~s solid by an effective modulus for the embedded inclusion. The accuracy of the indentation model is established by comparing the analytical results with detailed finite element simulations for various bi-material configurations of inclusion and substrate. The elastic indentation response is substantially influenced by the elastic modulus of the substrate, whereas the plastic response is dictated by the yield strength of the inclusion. The practical applicability of the indentation model is demonstrated by making use of the measured indentation response of an embedded paint sample, as reported in the literature, to deduce the elastic modulus of the paint.

Keywords: Nanoindentation, paint, resin, bi-material, elastic modulus, yield strength

---

1. Introduction

The indentation test is a widely used experimental technique for measuring material properties, such as elastic modulus [1, 2], yield strength and hardness [3, 4] and fracture toughness [5], over a wide range of length scales. The test entails the measurement of the force to press a shaped indenter tip into the surface of a sample; in principle, it is a simple test to perform but is notoriously difficult to interpret [6]. The application of this technique at the micro and nano scales can make~~s~~ it possible to ~~estimate the~~ measure the mechanical properties (modulus, strength and toughness) of small-scale material systems, such as thin coatings on a substrate [7, 8], individual crystalline grains of a metallic microstructure

---

Email address: `a.s.j.suiker@tue.nl` (A.S.J. Suiker)

[9, 10, 11], and small particles embedded in a supporting matrix [12, 13], ~~thereby measuring~~ and can allow for the measurement of potential size effects [14, 15, 16, 17, 18]. Due to the local character of an indentation measurement, indentation testing is suitable for determining the properties of a material for which a limited number of (small) samples are available, ~~e.g., the~~ for example paints that are used in valuable and historical paintings [19, 20, 21, 22, 23, 24].

Paint samples subjected to indentation are typically embedded in a relatively stiff, supporting resin. Several methods have been proposed for obtaining the elastic modulus of embedded samples from experimental indentation data. One method aims at finding the maximum indentation depth such that the measured unloading modulus can be accurately computed without due influence by the embedding material [9, 25, 26, 27]. Nevertheless, it is not always possible to limit the indentation depth to the small value required by this method, and consequently it is necessary to take the contribution to macroscopic compliance from the embedding material into account [28, 29, 12, 30, 21].

Accurate analytical and numerical solutions have been obtained for the elastic indentation of diverse heterogeneous material systems, such as coatings supported by a semi-infinite substrate [31, 32, 33] and bi-materials that contain a vertical material interface [34]. In [35] the elastic indentation of a hemispherical particle embedded at the free surface of a half space was studied, adopting the assumption that the indenter contact area remains relatively small with respect to the particle size. A first-order asymptotic solution of the Boussinesq-type problem was established, and the effect of the mismatch in elastic parameters on the indentation response was shown. However, much less is known about the relationship between Young's modulus and the macroscopic compliance of an embedded surface inclusion under relatively large indentations, as exhibited by indentation tests on embedded paint samples.

In the present study, an analytical model is derived to relate the elastic and plastic properties of an embedded hemispherical inclusion to its indentation response. The model differs from the approaches outlined above by starting from the analytical expressions for the elastic and elasto-plastic indentation responses of homogeneous materials, and adapting them by replacing the ~~homogeneous~~ modulus of the homogeneous solid by an effective modulus for the embedded sample. The effective modulus is derived from the analytical solution for the elastic response of a spherical cavity in a spherical particle, embedded in an infinite medium of different elastic properties. The cavity is subjected to a uniform, internal pressure. The accuracy of the analytical model is established by comparing the analytical indentation results for various bi-material configurations with those from detailed finite element simulations. The practical applicability of the indentation model is demonstrated by determining the elastic modulus of a paint from indentation measurements on an embedded paint sample as reported in the literature [21].

This paper is organized as follows. In Section 2 a review is provided of analytical elastic and elasto-plastic indentation models for homogeneous materials, and the accuracy of the analytical elasto-plastic indentation model is assessed by comparing its response to that obtained from finite element simulations. In Section 3 an analytical expression is derived for the effective modulus of a bi-material. In Section 4 this analytical expression is combined with the analytical indentation models for homogeneous materials reviewed in Section 2 to simulate the indentation response of elastic and elastic, ideally plastic bi-materials. The accuracy of the analytical models is assessed by comparison with detailed finite element simulations. In Section 5 the practical applicability of the analytical indentation model is demonstrated by determining the elastic modulus of an embedded paint sample from experimental indentation data. Finally, the main conclusions of the study are presented in Section 6 .

2. Review of indentation models for homogeneous materials

Similarity solutions have been developed for the indentation of a half space made from a power-law solid by a headshape of power-law form (such as a paraboloid or cone) [36, 37]. The force F applied to the indenter is related to the indentation depth h and alternatively to the indentation contact radius a by [2, 38, 39, 40, 41]

$$F = C_h h^m \qquad \text{and} \qquad F = C_a a^n \,, \tag{1}$$

where m, n, C_h and C_a depend upon the properties of the non-linear~~, deformation theory~~ solid and upon the geometry of the headshape.

In general, the values of m, n, C_h and C_a differ for loading and unloading, as unloading is usually associated with an elastic material response. ~~For example, for conical indentation of an elastic, ideally plastic solid, $m = 2$ for loading and $1 < m < 2$ for elastic unloading[1] (with $m = 2$ and $m = 1$ respectively representing the purely elastic and rigid-plastic limits), whereby the specific value during unloading depends on the geometry of the residual, plastic~~

~~[1] During elastic unloading of an elasto-plastic material, the indentation depth used in Eq.(1)$_1$ refers to the recoverable, elastic part, see also Eq.(10).~~

Alike, for the cone $m=2$ for both elastic and for rigid, ideally plastic solid. I do not see why unloading of an elastic-plastic indent gives a power low response (no reason that it should). Elastic unloading is reversible for an elastic solid.

~~indent generated during loading, which is determined by the ratio between the elastic modulus and the yield strength of the material [42].~~ The specific case of indentation of a linear elastic solid is treated in Section 2.1; elastic unloading of an indented elasto-plastic solid is discussed in Section 2.2, and indentation of an elastic, ideally plastic solid is considered in Section 2.3.

2.1. Indentation of an elastic solid

Consider a homogeneous, elastic half-space ~~solid~~ indented by a frictionless, rigid conical punch. Harding [43] and Sneddon [1, 2] showed that the force-displacement relations given by Eq. (1) are of the ~~specific~~ form

$$F = \frac{2\tan\alpha}{\pi}\frac{E}{1-\nu^2}h^2 \qquad \text{and} \qquad F = \frac{\pi}{2\tan\alpha}\frac{E}{1-\nu^2}a^2\,, \tag{2}$$

where α is the semi-apex angle of the indenter and E and ν are the Young's modulus and Poisson's ratio ~~of the half space~~, respectively. The elastic compliance of the indenter can be accounted for by replacing the plane-strain elastic modulus $E/(1-\nu^2)$ in the above two expressions by a reduced modulus E_r defined as [3, 38]

$$\frac{1}{E_r} = \frac{1-\nu^2}{E} + \frac{1-\nu_{in}^2}{E_{in}}\,, \tag{3}$$

where E_{in} and ν_{in} are the Young's modulus and Poisson's ratio of the indenter, respectively. Note from Eq.(2) that the exponents m and n in Eq.(1) have the value $m = n = 2$, and C_h and C_a are given by

$$C_h = \frac{2\,\tan\alpha}{\pi}\frac{E}{1-\nu^2} \qquad \text{and} \qquad C_a = \frac{\pi}{2\,\tan\alpha}\frac{E}{1-\nu^2}\,, \tag{4}$$

The geometrical parameters ~~and~~ h and a are related by

$$h = \frac{\pi a}{2\tan\alpha}\,. \tag{5}$$

As sketched in Figure 1, sink-in occurs at the edge of the indenter to a depth h_s, as a result of which the contact depth associated with no sink-in (or pile-up), $h_c = a/\tan\alpha$, is less than the true indentation depth h, such that

$$\frac{h_c}{h} = \frac{2}{\pi}\,. \tag{6}$$

via Eq.(4). The sink-in displacement h_s follows immediately from the identity

$$h = h_s + h_c, \tag{7}$$

an

$$h_s = \frac{(\pi-2)}{\pi} h$$ (8) xx

Note that, for an elastic indentation, the F(h) curve is reversible and the loading slope equals the unloading slope S. In contrast, for an elastic-plastic indentation, the elastic unloading slope S exceeds that of the elastic-plastic loading slope.

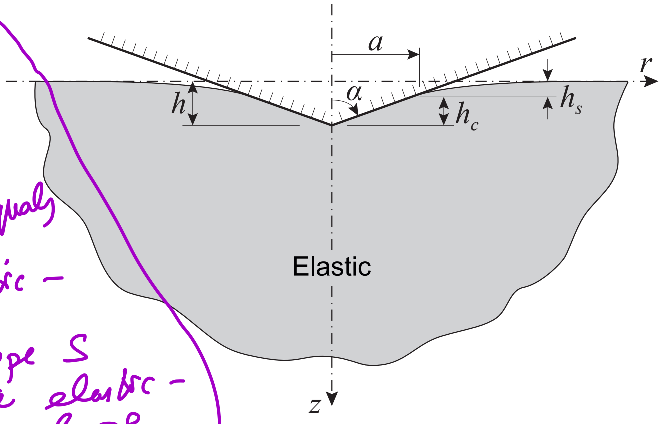

Figure 1: Indentation of a homogeneous, elastic material over a depth h, using an indenter with semi-apex angle α. The contact radius, contact depth and sink-in displacement are given by a, h_c, and h_s, respectively.

initial value of unloading

The ~~incremental~~ contact stiffness ~~$S = \hat{S}(h)$~~ $S(h)$ is the derivative of Eq.(2)$_1$ with respect to the indentation depth h:

$$S = \frac{\partial F}{\partial h} = \frac{4 \tan \alpha}{\pi} \frac{E}{1 - \nu^2} h \,. \tag{8}$$

Upon inserting Eq.(5) into Eq.(8) and defining the projected contact area as $A_p = \pi a^2$, the Young's modulus E is related to S via [38, 40, 44]

$$E = \frac{\sqrt{\pi}}{2} \frac{S(1 - \nu^2)}{\sqrt{A_p}} \,. \tag{9}$$

The right-hand side of the above expression needs to be multiplied by a correction factor $1/\zeta$ ~~in case~~ when the projected contact area A_p is non-circular, with ζ equal to 1.012 and 1.034 for, respectively, square and triangular shape indents [45].

2.2. Elastic unloading of an elasto-plastic solid

Equation (9) can be used to determine the Young's modulus from indentation tests on an elasto-plastic solid by following the procedure of Oliver and Pharr [38, 40], summarized as follows. Assume that the indent is elasto-plastic in nature but unloading is elastic from an indentation depth $h = h_{max}$ to a residual depth h_f at zero load, see Figure 2. Equation (1)$_1$ is used to fit the unloading curve ~~from~~ over the recoverable, elastic indentation ~~depth~~ interval $(h_{max} - h_f)$ as

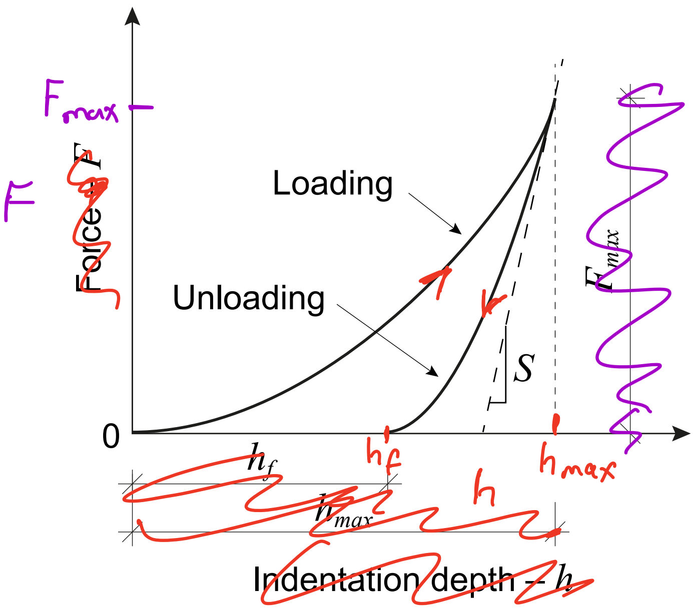

Figure 2: Schematic representation of the loading and unloading stages in an indentation experiment. During loading, the load F is increased from zero to a value F_{max}, whereby the indentation h obtains a value h_{max}. Under subsequent unloading, the indentation depth decreases towards a residual, plastic indent h_f at zero load. The reversible, elastic indentation experienced during unloading is $(h_{max} - h_f)$. The elastic contact stiffness at the onset of unloading is S. This figure is based upon a representation presented in [38].

[38, 40]

$$F = C_h (h - h_f)^m \,. \tag{10}$$

From the calibrated curve Eq.(10), the unloading contact stiffness S at the indentation depth $h = h_{max}$ is computed as

$$S = \left. \frac{\partial F}{\partial h} \right|_{h=h_{max}} = m C_h (h_{max} - h_f)^{m-1} \,. \tag{11}$$

Oliver and Pharr [40, 42] further assumed that the sink-in displacement h_s is purely elastic such that $m = 2$ and thus for a conical indenter, ~~via Eqs.(6) and (7)~~ m equals 2, and h_s is related to the ~~elastic~~ recoverable indentation ~~depth~~ interval $(h_{max} - h_f)$ ~~as~~ in a manner analogous to (8)xx such that

$$h_s = \frac{(\pi - 2)}{\pi} (h_{max} - h_f) \;. \tag{12}$$

upon making use of Eqs.(6) and (7).

Additionally, by inserting the exponent $m = 2$ for elastic indentation in Eqs.(10) and (11), it follows ~~from these expressions~~ that the initial elastic ~~contact~~ unloading stiffness S at $h = h_{max}$ reads

$$S = \frac{2 F_{max}}{(h_{max} - h_f)} \,, \tag{13}$$

~~with~~ where F_{max} is the indentation force at the indentation depth h_{max}. Now ~~C~~combin~~ing~~e Eqs.(7), (12) and (13) to obtain ~~then provides the following expression for the contact depth h_c:~~

$$h_c = h_{max} - h_s = h_{max} - \xi \, \frac{F_{max}}{S} \, , \tag{14}$$

with the unloading contact stiffness S of the elasto-plastic solid given by the general expression, Eq.(11), and $\xi = 2(\pi - 2)/\pi = 0.73$ for a conical indenter. A slightly lager value of $\xi = 0.75$ needs to be selected when the effective indenter shape during unloading is (accurately) approximated by a paraboloid of revolution [42]. The projected contact area A_p is determined from the value of h_c as deduced from Eq.(14), using the fitting procedure described in [38]. Alternatively, the contact area can be measured directly by imaging of the residual indent [38, 40]. Finally, the values of A_p and S are inserted into Eq.(9) to obtain the Young's modulus E of the indented solid, while the hardness follows from $H = F_{max}/A_p$.

2.3. Indentation of an elastic, ideally plastic solid

Marsh [46] and Johnson [3, 47] assumed that conical indentation of an elastic, ideally plastic solid by a rigid, conical indenter can be idealized by the expansion of an internally pressurised, hemispherical cavity from a vanishing initial radius to a current radius equal to the contact radius a, see Figure 3. The stress state $\boldsymbol{\sigma}$ inside the void (or "core") is a uniform pressure, $\boldsymbol{\sigma} = -p\boldsymbol{I}$, where $\boldsymbol{I}$ is the usual second-order identity tensor. The deformation state external to the hemispherical core is taken to be the same as that for an elastic, ideally plastic full space containing a spherical cavity of radius a and subjected to an internal pressure p [48]. The plastic zone extends from the core to an outer elastic-plastic boundary at a radius $r = c$, with $c > a$. At the interface $r = a$ between core and plastic zone, the radial stress in the plastic zone equals the hydrostatic stress p in the core. In addition, the radial displacement at the interface is compatible with the volume displaced by the conical indenter, assuming that the material within the core is incompressible. It is also ~~further~~ assumed that no pile-up or sink-in ~~of material~~ occurs during indentation, such that the indentation depth is $h = h_c = a/\tan\alpha$, see Figure 3.

Write σ_y as the yield strength of the indented material and $\beta = (90^\circ - \alpha)$ as the inclination of the conical indenter. Then, the mean indentation pressure p_m under the indenter is given

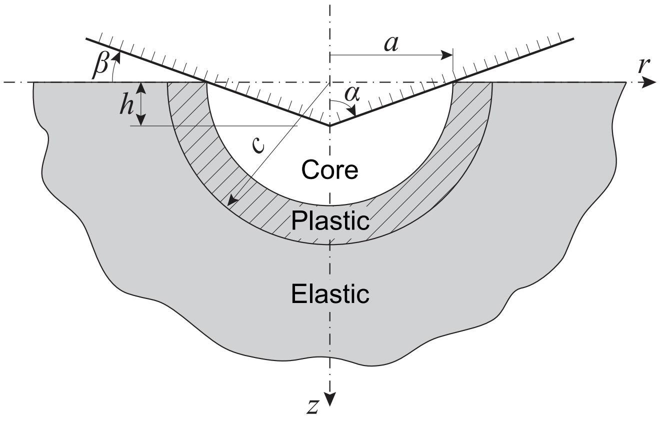

Figure 3: Cavity expansion indentation of a homogeneous, elastic, ideally plastic material to a depth h, using an indenter with semi-apex angle α. Indentation produces a hemispherical core of a radius equal to the contact radius a. The stress generated inside the core induces a hemispherical plastic zone of radius c.

by [3, 47]:

$$\frac{p_m}{\sigma_y} = \begin{cases} \dfrac{p}{\sigma_y} + \dfrac{2}{3} & \text{for} \quad 2 \leq \dfrac{E\tan\beta}{\sigma_y} \leq 27, \\[2ex] 2.8 \quad \text{for} & \dfrac{E\tan\beta}{\sigma_y} > 27\,, \end{cases} \tag{15}$$

where

$$\frac{p}{\sigma_y} = \frac{2}{3}\left(1 + \ln\left(\frac{1}{3}\frac{E\tan\beta}{\sigma_y}\right)\right)\,,$$

Equations

~~In which Eqs.~~(15)$_1$ and (15)$_2$, respectively, define the elasto-plastic and fully plastic indentation responses, r.

Note from Eq.(15) that the mean indentation pressure p_m is fully determined by the dimensionless parameter $(E\tan\beta)/\sigma_y$, which can be interpreted as the ratio of the representative strain imposed by the indenter, $\tan\beta$, and the yield strain, σ_y/E [3]. The use of alternative headshapes of indenters (spherical, Vickers, Berkovich) somewhat changes the point of first yield and full yielding in Eq.(15), but preserves the overall form of Eq.(15) [3]. Although the solution given by Eq.(15) is based upon the assumption that the indented solid is incompressible, the effect of the value of Poisson's ratio upon the elasto-plastic response is minor [3, 47]. The compliance of the indenter is taken into account ~~upon~~ by replacing the Young's modulus E in Eq.(15) by the reduced modulus E_r as given by Eq.(3) [3, 47]. The force F on the conical indenter follows directly from the mean indentation pressure p_m and the projected contact area $A_p = \pi a^2$, such that

$$F = p_m \, A_p \, , \tag{16}$$

and consequently the constant C_a in the general expression, Eq.$(1)_2$, specializes to $C_a = \pi p_m$, with p_m given by Eq.(15), and the exponent $n = 2$. Further, from the relation $h = a/\tan\alpha$, the parameters C_h and m in Eq.$(1)_1$ follow as $C_h = \pi p_m (\tan\alpha)^2$ and $m = 2$.

Three-dimensional indentation simulations reveal that Johnson's cavity expansion model gives a rather good representation of the nominal hardness of polymers (e.g., paints); an approximately spherical plastic zone develops and no material pile-up occurs next to the indenter [49, 50]. In order to verify the accuracy of Eq.(15), the results of this model are ~~first~~ compared to large deformation Finite Element (FE) simulations of the indentation of an elastic, ideally plastic half space, using the commercial FE package ABAQUS Standard[2]. The indentation problem is modelled as axisymmetric, with the vertical line of symmetry passing through the centre of the indenter.

The indented solid is discretized using axisymmetric, 4-node, iso-parametric elements with ~~a~~ 2 × 2 Gaussian quadrature. The conical indenter is modelled as rigid and frictionless, and is characterized by a semi-apex angle of $\alpha = 70.3°$, corresponding to an inclination $\beta = 19.7°$ of the indenter. The numerical stability of the solution is enhanced by slightly rounding off of the indenter tip ~~through the application of~~ with a small, finite tip radius. The ~~application~~ inclusion of a tip radius also makes the indenter more representative of a practical conical indenter. The indenter is displaced vertically into the solid using an incremental time-marching scheme with an automatic time-step adaptation. The maximum indentation depth is set to 8 µm, which is a factor of 6.25 smaller than the radial and vertical dimensions of 50 µm defining the axisymmetric finite element configuration. A so-called node-to-surface contact criterion is adopted in order to rigorously check for new contacts between the indenter and the elements that define the top surface of the solid.

The FE mesh is refined near the indenter tip, and the semi-infinite character of the solid is simulated by placing 4-node infinite elements with an elastic material behaviour along the lateral and lower boundaries of the finite element geometry [51]. The converged FE discretization deduced from the above mesh refinement study corresponds to a spatial discretization of 4499

---

[2] Dassault Systems Simulia Sorp., Providence, RI, USA.

finite elements and 100 infinite elements. The choice of element discretization is determined from a preliminary mesh refinement study on the initial, elastic indentation response, ~~upon noting that elastic deformation in the vicinity of the indenter tip extends over a relatively restricted domain.~~ In the mesh refinement study the elastic response was simulated by selecting an almost incompressible solid with $\nu = 0.499$; the converged numerical results agree with the analytical solution given by Eq.(2) to within an acceptable inaccuracy of 1%.

In the FE simulations of the indentation of the elastic, ideally plastic solid the mesh density of the converged elastic solution is preserved and the size of the mesh is increased by a factor of 10 in the radial and vertical directions to ensure that the plastic zone generated by the conical indenter does not reach the elastic infinite elements located at the perimeter of the FE model. Consequently, the number of finite elements in this FE model equals 15 space 557. The number of infinite elements is kept the same as in the mesh convergence study, ~~i.e.,~~ that is 100. The Poisson's ratio of the solid $\nu = 0.35$ is representative of various solids, including historical paints [52]. J_2-flow theory is used for the plastic response, and the Young's modulus E and yield strength σ_y are selected such that the dimensionless parameter $(E \tan\beta)/\sigma_y$ appearing in Eq.(15) is varied stepwisely from 1 to 100, ~~in correspondence with~~ corresponding to 100 separate FE simulations.

Figure 4 shows a comparison between the results obtained from the FE simulations (grey circles and black solid line) and Johnson's cavity expansion model, Eq.(15), (dashed line). Each vertical column of data points, designated by the grey circles, correspond~~s~~ to an increase in indentation depth h for an integer number of contact nodes. The bottom point of each column of data points gives the instant at which a new node comes into contact with the indenter. Thus, the contact radius a remains constant and the mean indentation pressure p_m (plotted along the vertical axis) grows until the next node makes contact. This feature of mesh discretization repeats itself and a new column of vertical data points is generated, see also [53, 54, 55]. The black solid line depicted in Figure 4 captures the mean values of the vertical columns of data points. The cavity expansion model, Eq.(15), is in reasonable agreement with the response of the FE simulations, with an underprediction in the intermediate elasto-plastic regime and an overprediction in the final, plastic regime. Although not illustrated here, the FE results also show that the ratio of contact depth h_c to indentation depth h in the elasto-plastic regime monotonically increases ~~from $h_c/h = 2/\pi$ to $h_c/h = 1$~~: the initial, elastic value is in agreement with the expression given by Eq.(6). When $(E \tan\beta)/\sigma_y$ exceeds 27 the plastic deformation regime is reached, the mean indentation pressure p_m becomes constant, and the

delete to eliminate the inconsistency.

inconsistent.

contact depth develops with $h_c/h > 1$, indicating that material piles up next to the indenter, as previously discussed [3, 47].

Additional comparisons between the results of the cavity expansion model and those of FE simulations can be found in [47], including a comparison of the subsurface and surface stress fields in Figures 6.15 and 6.16, which shows good agreement.

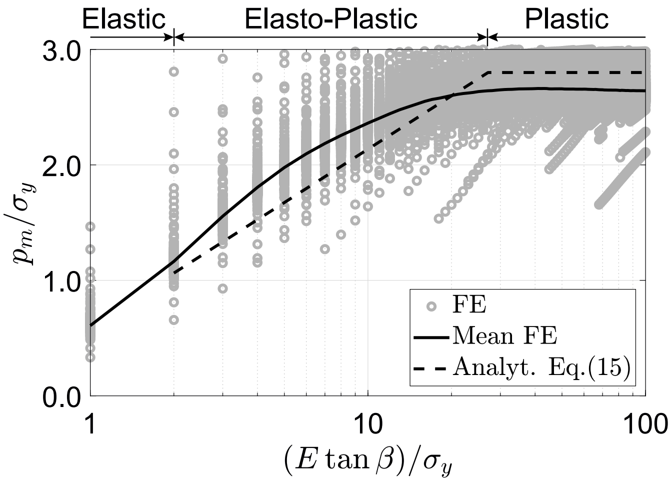

Figure 4: Indentation response of an elastic, ideally plastic solid. Mean indentation pressure p_m normalized by the yield strength σ_y as a function of the dimensionless parameter $(E \tan\beta)/\sigma_y$. The figure shows the FE response (grey circles), the mean FE response (solid black line) and the prediction by the cavity expansion model, Eq.(15) (dashed line).

3. Closed-form expression for the effective elastic modulus of a bi-material

The indentation model for a homogeneous solid reviewed in Section 2 will be adapted to the case of a bi-material composed of a hemispherical inclusion at the surface of a dissimilar half space, with the indent placed at the centre of the inclusion. As will be demonstrated in Section 4, this adaptation will be achieved via an effective elastic modulus of the bi-material, followed by taking this effective modulus as the value of Young's modulus in an indentation model for a homogeneous solid. In the present section an analytical expression for the effective elastic modulus is derived from the response of a hollow, spherical particle embedded in an infinite medium of dissimilar elastic properties, and subjected to a uniform, internal pressure, see Figure 5. The elastic displacement field in the bi-material is derived in Section 3.1, and an analytical expression for the effective elastic modulus is obtained in Section 3.2.

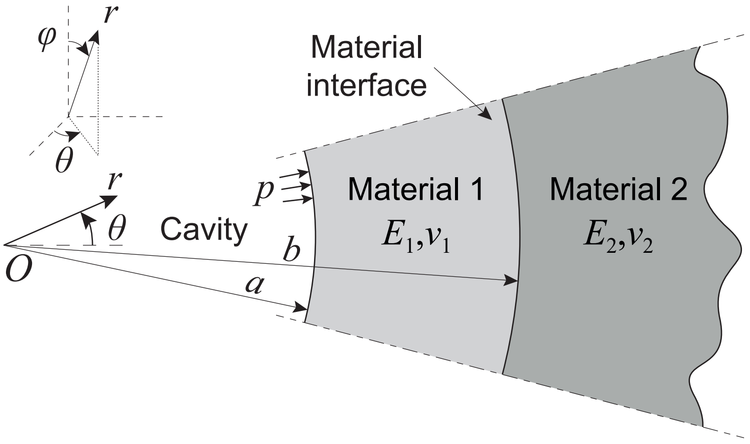

Figure 5: A spherical shell of outer radius b (material 1) embedded in an infinite medium (material 2). The spherical cavity of radius a is pressurized by a uniform pressure p. The inset shows the spherical coordinate system (r, θ, φ), with $r \geq a$ the radial coordinate of a material point, θ the polar angle coordinate, and φ the azimuth angle coordinate.

3.1. Elastic displacement field

The geometry depicted in Figure 5 is characterized by an elastic spherical shell of outer radius b (material 1) that is embedded in an infinite solid of dissimilar elastic properties (material 2). The spherical cavity of radius a is subjected to an internal uniform pressure p. A spherical coordinate system (r, θ, φ) is adopted, where $r \geq a$ is the radial coordinate, θ the polar angle coordinate, and φ is the azimuth angle coordinate. Upon exploiting the spherical symmetry of the problem, the following equilibrium and kinematic conditions hold:

$$\begin{aligned}
&\sigma_{r\theta} = \sigma_{r\varphi} = \sigma_{\theta\varphi} = 0\,, \\
&\sigma_{\theta\theta} = \sigma_{\varphi\varphi}\,, \\
&u_\theta = u_\varphi = 0\,, \\
&\varepsilon_{r\theta} = \varepsilon_{r\varphi} = \varepsilon_{\theta\varphi} = 0\,, \\
&\varepsilon_{\theta\theta} = \varepsilon_{\varphi\varphi}\,.
\end{aligned} \tag{17}$$

Here, σ_{mn}, ε_{mn} and u_m are the stress, strain and displacement components in the spherical coordinate system. The constitutive relations and the remaining equilibrium and kinematic relations of the solid are

$$\begin{aligned}
&\sigma_{rr} - 2\nu_i \sigma_{\theta\theta} = E_i \, \varepsilon_{rr} \, , \\
&\sigma_{\theta\theta}(1-\nu_i) - \nu_i \sigma_{rr} = E_i \, \varepsilon_{\theta\theta} \, , \\
&\frac{\partial \sigma_{rr}}{\partial r} + \frac{2}{r}(\sigma_{rr} - \sigma_{\theta\theta}) = 0 \, , \\
&\varepsilon_{rr} = \frac{\partial u_r}{\partial r} \, , \\
&\varepsilon_{\theta\theta} = \frac{u_r}{r} ,
\end{aligned} \tag{18}$$

where E_i and ν_i are the Young's modulus and Poisson's ratio of material $i \in \{1, 2\}$. Additionally, the boundary conditions (at $r = a$ and $r \to \infty$) and interfacial conditions (at $r = b$) are given by:

$$\begin{aligned}
\sigma_{rr}(r = a) &= -p \, , \\
u_r(r \to \infty) &= 0 \, , \\
\sigma_{rr,1}(r = b) &= \sigma_{rr,2}(r = b) \, , \\
u_{r,1}(r = b) &= u_{r,2}(r = b) \, ,
\end{aligned} \tag{19}$$

in which the comma and subindices 1 and 2 used in the definition of the interfacial conditions Eq.$(19)_{3,4}$ refer to materials 1 and 2, respectively. Combining Eqs.(18) and (19) leads to the following expression for the radial displacement:

$$u_r(r) = \begin{cases} \dfrac{a^3 p \left(2\left(b^3 - r^3\right) E_2 \left(2\nu_1^2 + \nu_1 - 1\right) - E_1 \left(b^3 + 2r^3 + \left(b^3 - 4r^3\right)\nu_1\right)\left(1+\nu_2\right)\right)}{2r^2 E_1 \left(-E_2\left(a^3 + 2b^3 + \left(a^3 - 4b^3\right)\nu_1\right) + \left(a^3 - b^3\right) E_1 \left(1+\nu_2\right)\right)} \\ \quad \text{for } a \leq r \leq b, \\ \dfrac{3a^3 b^3 p \left(-1+\nu_1\right)\left(1+\nu_2\right)}{2r^2 \left(-E_2\left(a^3 + 2b^3 + \left(a^3 - 4b^3\right)\nu_1\right) + \left(a^3 - b^3\right) E_1 \left(1+\nu_2\right)\right)} & \text{for } r > b. \end{cases} \tag{20}$$

For the specific case of a vanishing material 2 (i.e., $E_2 = 0$, $\nu_2 = 0$), Eq.(20) reduces to:

$$u_r(r) = \frac{a^3 p (b^3 + 2r^3 + (b^3 - 4r^3)\nu)}{2(b^3 - a^3) r^2 E} \quad \text{with } a \leq r \leq b, \tag{21}$$

in which the subscripts of the elastic parameters E_1 and ν_1 have been dropped for the sake of clarity. Equation (21) gives the elastic displacement field for a homogeneous spherical shell of finite thickness $(b - a)$, with a free outer boundary at $r = b$, and loaded by a uniform pressure p at its inner boundary $r = a$; this expression is in agreement with that given in [48]. For the special case of an internally pressurized spherical cavity in an infinite, homogeneous medium, i.e., $E_1 = E_2 = E$ and $\nu_1 = \nu_2 = \nu$, Eq.(20) reduces to the classical solution [56]:

$$u_r(r) = \frac{a^3 p(1+\nu)}{2r^2 E} \qquad \text{with } r \geq a. \tag{22}$$

3.2. Effective elastic modulus of an embedded spherical shell

It follows from Eqs.$(18)_4$ and (22) that, for the case of a homogeneous infinite medium, the radial strain at the boundary $r = a$ of the cavity can be written as

$$\varepsilon_{rr}(r=a) = \frac{-p(1+\nu)}{E}, \tag{23}$$

which, upon rearrangement, expresses the Young's modulus as a function of the radial strain at $r = a$:

$$E = \frac{-p(1+\nu)}{\varepsilon_{rr}(r=a)}. \tag{24}$$

The assumption is made that the embedded spherical shell can be idealized by an equivalent cavity of radius a in a homogeneous full space by introducing an effective modulus $\bar{E}$ for the cavity in a homogeneous full space. The calibration is based on the assumption that the radial strain at the boundary $r = a$ of the cavity is the same for the two cases. Thus, the effective modulus $\bar{E}$ for the cavity in a homogeneous full space is defined by rearrangement of the above equation to read:

$$\bar{E} \equiv \frac{-p(1+\nu_1)}{\varepsilon_{rr}(r=a)}. \tag{25}$$

Here, the value of the radial strain at the boundary $r = a$ is for the embedded spherical shell, and is determined from Eqs.$(18)_4$ and $(20)_1$ as

$$\varepsilon_{rr}(r=a) = \frac{-p\left(\left(2b^3+a^3\right)E_2\left(2\nu_1^2+\nu_1-1\right) - E_1\left(b^3-a^3+\left(b^3+2a^3\right)\nu_1\right)(1+\nu_2)\right)}{E_1\left(-E_2\left(a^3+2b^3+\left(a^3-4b^3\right)\nu_1\right)+\left(a^3-b^3\right)E_1\left(1+\nu_2\right)\right)}. \tag{26}$$

Now insert Eq.(26) into Eq.(25) to obtain the effective elastic modulus:

$$\bar{E} = \frac{E_1(-E_2(a^3+2b^3+(a^3-4b^3)\nu_1)+(a^3-b^3)E_1(1+\nu_2))(1+\nu_1)}{(a^3+2b^3)E_2(2\nu_1^2+\nu_1-1) - E_1(-a^3+b^3+(2a^3+b^3)\nu_1)(1+\nu_2)}. \tag{27}$$

As required, This expression reduces to the Young's modulus of a homogeneous material, $\bar{E} = E$, when $E_1 = E_2 = E$ and $\nu_1 = \nu_2 = \nu$. In Section 4 the above expression for the effective elastic modulus of the bi-material ~~will be~~ is combined with the indentation models for homogeneous materials reviewed in Section 2 to ~~simulate~~ obtain analytical expressions for the indentation response of elastic and elasto-plastic bi-materials.

Note that an alternative expression for the effective modulus of the bi-material can be obtained by suitable matching of the hoop strain of the bi-material problem and the cavity in an effective, homogeneous full space at $r = a$. Combine Eqs.$(18)_5$ and (22) for the cavity in a homogeneous full space, and substitute E by $\bar{E}$ and ν by ν_1:

$$\bar{E} \equiv \frac{p(1+\nu_1)}{2\,\varepsilon_{\theta\theta}(r=a)} \,. \tag{28}$$

Then, assume that the value of $\varepsilon_{\theta\theta}(r = a)$ for the embedded spherical shell equals that for the equivalent effective full space. A ~~preliminary~~ comparison study ~~not presented here revealed~~ has been performed between the use of hoop and radial strain components to obtain $\bar{E}$, but is not detailed here. It is found that the effective modulus $\bar{E}$ based on Eq.(25) provides a more accurate estimate of the elastic indentation response of an embedded hemispherical inclusion than that based on Eq.(28).

4. Indentation of embedded hemispherical particles

The closed-form expression for the effective elastic modulus of the bi-material, Eq.(27), is now combined with the analytical indentation models for homogeneous materials, as reviewed in Section 2. First, the indentation of an *elastic* hemispherical particle embedded in an elastic half space is reported in Section 4.1. Second, the indentation of an *elastic, ideally plastic* hemispherical particle embedded in an elastic half space is given in Section 4.2. In each section, the accuracy of the analytical models is established by comparing analytical predictions with detailed finite element simulations.

4.1. Indentation of an elastic hemispherical particle embedded in an elastic half space

The elastic indentation of a hemispherical particle embedded in a half space of differing elastic properties is sketched in Figure 6. The analytical indentation model makes use of Eq.(27) in the F-a relation, Eq.$(2)_2$. Accordingly, the indentation force F on the rigid conical indenter is expressed in terms of the contact radius a of the bi-material as

$$F = \gamma \frac{\pi}{2\tan\alpha} \frac{\bar{E}}{(1-\nu_1^2)} a^2, \tag{29}$$

in which the Poisson's ratio corresponds to that of the indented material 1. Equation (29) has been extended by a factor γ, which corrects for a small, artificial overlap between the geometry

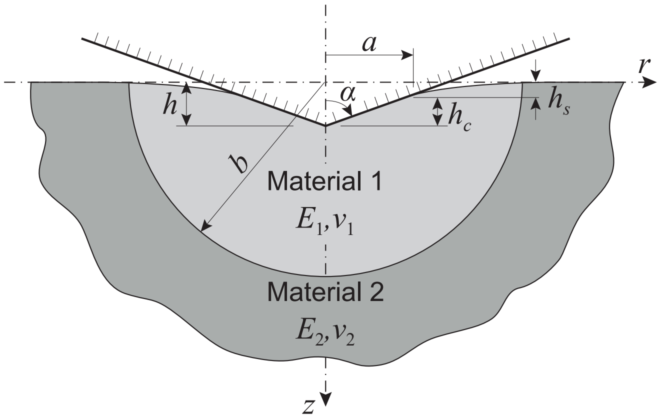

Figure 6: Indentation of an elastic hemispherical particle of radius b (material 1) embedded in an elastic half space (material 2), using an indenter ~~with~~ of semi-apex angle α. The contact radius a, contact depth h_c and sink-in depth h_s each depend upon the indentation depth h.

of the rigid indenter and the deformed material surface, as characteristic of Sneddon's solution, see also [57]. An analytical expression for the factor γ is obtained by calibrating Eq.(29) on the FE indentation response of a homogeneous material - here designated as "material 1" - with the Poisson's ratio taking values in the range of 0 to 0.5. The FE mesh used for the axisymmetric indentation models corresponds to that ~~followi~~ng from the mesh convergence study described in Section 2.3. The calibration of the factor γ is performed when the indentation response has converged towards a steady state, as characterized by on almost ~~a (virtuall~~y) constant value of the dimensionless indentation force $F/(A_pE_1)$, with $A_p = \pi a^2$ the projected contact area. The value of γ is taken as the average of the values calibrated for a range of contact radii a. Figure 7 illustrates that the numerical values for γ are accurately captured by the linear relation

$$\gamma = 1.2 - 0.4\nu_1\,. \tag{30}$$

Note that $\gamma = 1$ in the limit of an incompressible material, $\nu = 0.5$, which is the case that has been selected for the mesh refinement study discussed Section 2.3.

4.1.1. Elastic indentation response

The elastic indentation response of the bi-material configuration sketched in Figure 6 is illustrated in Figure 8. Specifically, the dimensionless indentation force $F/(A_pE_1)$ is plotted as a function of the dimensionless indentation radius a/b for three values of modulus mismatch, $E_2/E_1 = [0.2, 1.0, 5.0]$, and 6 choices of Poisson ratios, $\nu_1 = \nu_2$ in the range of 0 to 0.5. The black solid line represents the FE response, which develops in a sawtooth fashion due to the

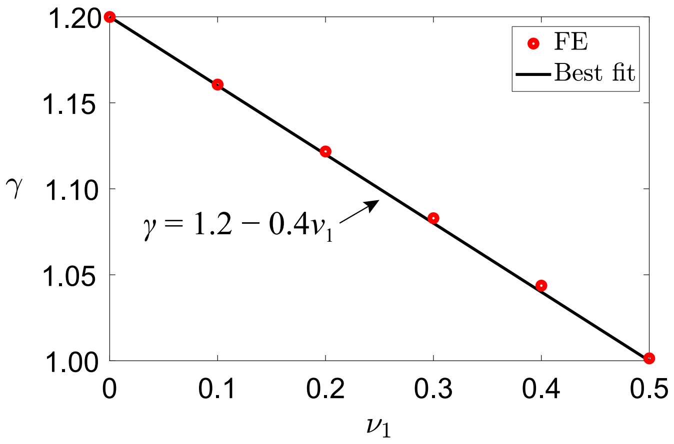

Figure 7: Analytical expression for the factor γ (black line) as given by Eq.(30), which is obtained from calibrating Eq.(29) for a homogeneous material to the results of FE simulations (red circles) for selected values of Poisson's ratio ν_1.

fact that the contact condition of the indenter is prescribed in a spatially discrete manner via the individual finite element nodes, see also Figure 4 and the explanation provided in Section 2.3. The mean of the FE sawtooth curve is given by the red dotted line. The analytical model, Eq.(29), with γ and $\bar{E}$ respectively given by Eqs.(30) and (27), is represented by the black dashed line. Additionally, for the specific case of $E_2/E_1 = 0.2$, the analytical model with an effective modulus for an *incompressible* bi-material is depicted in Figures 8(a)-(f) by the black dotted line; the corresponding expression for the effective modulus follows from inserting $\nu_1 = \nu_2 = 0.5$ into Eq.(27):

$$\bar{E} = \bar{E}_{inc} = \frac{E_1\left(b^3 - a^3\right) + E_2 a^3}{b^3}\,, \tag{31}$$

with the subscript "*inc*" referring to "incompressible". This expression correctly reduces to $\bar{E}_{inc} = E_1$ for a homogeneous material, $E_2/E_1 = 1$. The analytical indentation model, Eq.(29), that uses the effective modulus of the incompressible material, Eq.(31), henceforth will be denoted "analytical model for the incompressible bi-material"; the indentation model also describes indented materials with a Poisson's ratio ν_1 different from 0.5, via the terms $\gamma = 1.2 - 0.4\nu_1$ and $(1 - \nu_1^2)$ in Eq.(29).

For the case $E_2/E_1 = 0.2$ of a stiff particle embedded in a soft matrix, the mean FE results plotted in Figure 8 show that the dimensionless indentation force $F/(A_p E_1)$ monotonically decreases with increasing indentation radius a/b after a relatively short initiation phase[3]. In

---

[3] The FE results shown in Figure 8 are characterized by a short ~~initiation~~ initial phase, during which the round indenter tip establishes contact with the material surface and the dimensionless indentation force $F/(A_p E_1)$

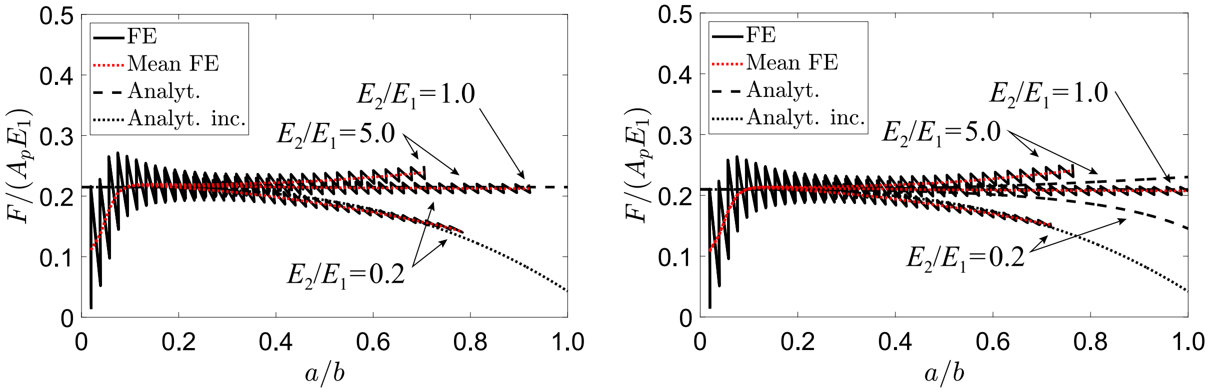

(a) $\nu_1 = \nu_2 = 0.0$ (b) $\nu_1 = \nu_2 = 0.1$

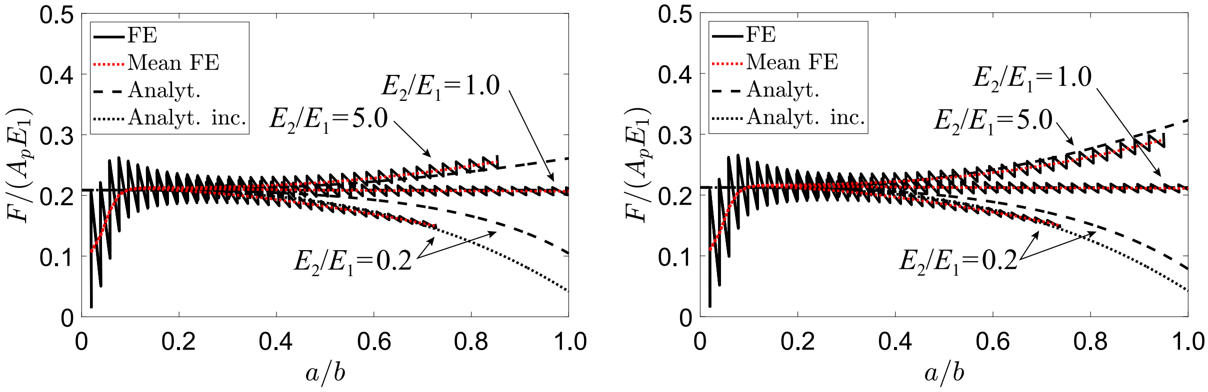

(c) $\nu_1 = \nu_2 = 0.2$ (d) $\nu_1 = \nu_2 = 0.3$

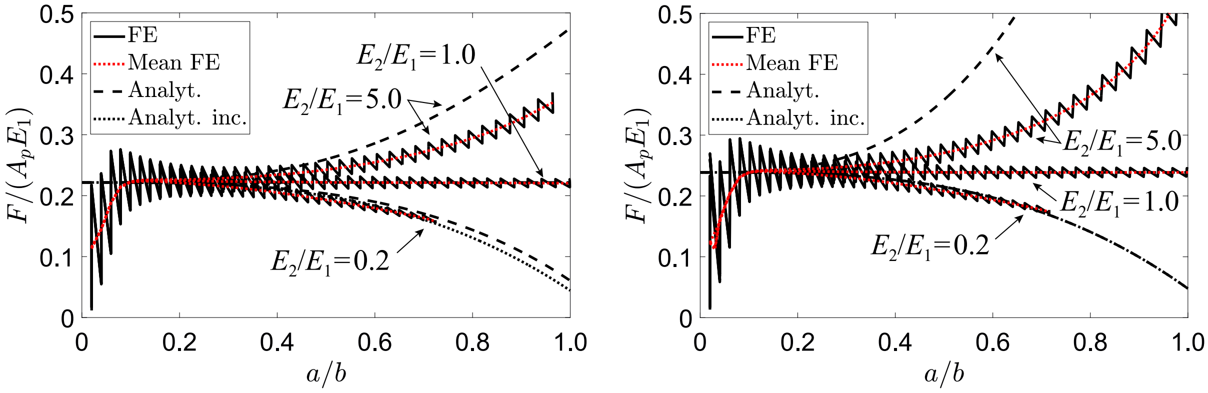

(e) $\nu_1 = \nu_2 = 0.4$ (f) $\nu_1 = \nu_2 = 0.5$

Figure 8: Indentation response of an elastic hemispherical particle embedded in an elastic half space. Dimensionless indentation force $F/(A_pE_1)$ versus dimensionless indentation radius a/b, as calculated by FE simulations (black solid line), the analytical model Eq.(29) with the general stiffness expression Eq.(27) (black dashed line), and the analytical model Eq.(29) with the stiffness expression for an incompressible material Eq.(31) (black dotted line). The mean FE response is represented by the red dotted line. The results are shown for three values of modulus mismatch, $E_2/E_1 = 0.2$, 1.0, and 5.0, and for (a) $\nu_1 = \nu_2 = 0.0$, (b) $\nu_1 = \nu_2 = 0.1$, (c) $\nu_1 = \nu_2 = 0.2$, (d) $\nu_1 = \nu_2 = 0.3$, (e) $\nu_1 = \nu_2 = 0.4$, (f) $\nu_1 = \nu_2 = 0.5$.

contrast, for a homogeneous material, $E_2/E_1 = 1.0$, $F/(A_pE_1)$ is independent of a/b, and for the case $E_2/E_1 = 5.0$ of a compliant particle embedded in a stiff matrix $F/(A_pE_1)$ increases

---

increases.

monotonically with a/b. Remarkably, the indentation load for the stiff particle configuration, $E_2/E_1 = 0.2$, is almost insensitive to the choice of Poisson's ratios ν_1 and ν_2, and is adequately captured by the analytical model for an incompressible bi-material, Eq.(31). The analytical model with the general stiffness expression, Eq.(27), overpredicts the FE results for this case, although the discrepancy decreases for a larger value of Poisson's ratios, and eventually vanishes in the limit of an incompressible bi-material, $\nu_1 = \nu_2 = 0.5$. For a homogeneous material, $E_2/E_1 = 1$, the analytical models with the stiffness expressions given by Eqs.(27) and (31) lead to an identical result, and accurately describe the mean FE response. For the compliant particle configuration, $E_2/E_1 = 5.0$, the analytical model with the general stiffness expression Eq.(27) gives close agreement with the mean FE results over the full range of dimensionless indentation radii a/b in case of moderate values of the Poisson's ratios, $0.2 \leq \nu_i \leq 0.3$ and $i \in \{1, 2\}$. Since this range includes the Poisson ratios of many engineering materials, it is concluded that this analytical indentation model is of practical value. For values of Poisson ratios falling outside this range, Figure 8 shows that the analytical model only provides accurate results up to a normalized indentation radius of $a/b \approx 0.3$ to 0.4, and for larger indentation values may significantly underpredict (for $\nu_1, \nu_2 < 0.2$) or overpredict (for $\nu_1, \nu_2 > 0.3$) the mean FE response of the compliant particle configuration. Finally, note from Figure 8(f) that, for $E_2/E_1 = 5.0$, the analytical model for the incompressible bi-material deviates from the FE results obtained for a Poisson's ratio of 0.5, which is the reason that analytical predictions for an incompressible bi-material with $E_2/E_1 = 5.0$ have been omitted from Figures 8(a)-(e).

4.1.2. Effective elastic modulus

The mean FE results indicated by the red dotted line in Figure 8 can be used to compute the normalized effective elastic modulus $\bar{E}/E_1$ of the bi-material from the inverse relation of Eq.(29), i.e.,

$$\frac{\bar{E}}{E_1} = \frac{2\tan\alpha}{\gamma}\frac{F(1-\nu_1^2)}{A_p E_1}\,. \tag{32}$$

Accordingly, in Figures 9(a)-(f) the effective modulus following from the FE simulations is compared to the effective modulus, Eq.(27), and the effective modulus for the incompressible bi-material, Eq.(31), by plotting the dimensionless value $\bar{E}/E_1$ against the dimensionless indentation radius a/b for three values of stiffness mismatches $E_2/E_1 = [0.2, 1.0, 5.0]$ and six values of Poisson ratio over the range 0 to 0.5. After a minor initiation phase, all curves attain an effective modulus of $\bar{E} = E_1$, which confirms that at small indentation the effective mod-

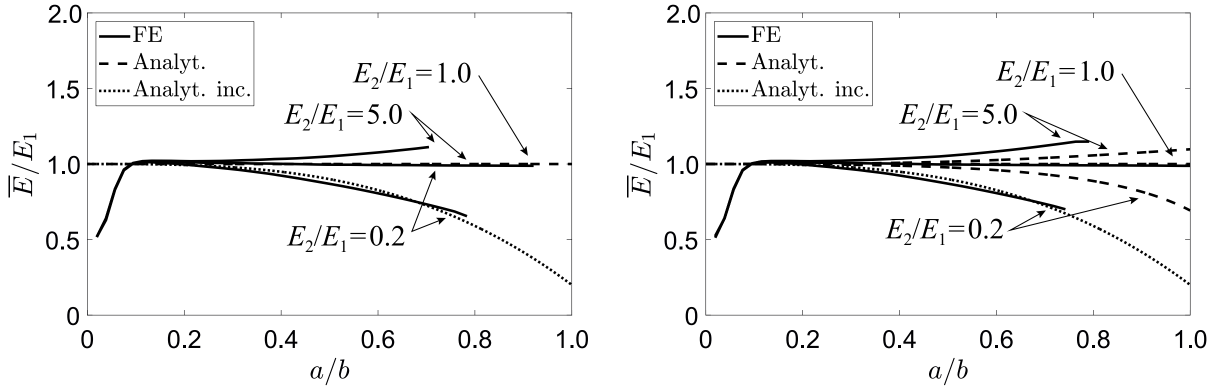

(a) $\nu_1 = \nu_2 = 0.0$ (b) $\nu_1 = \nu_2 = 0.1$

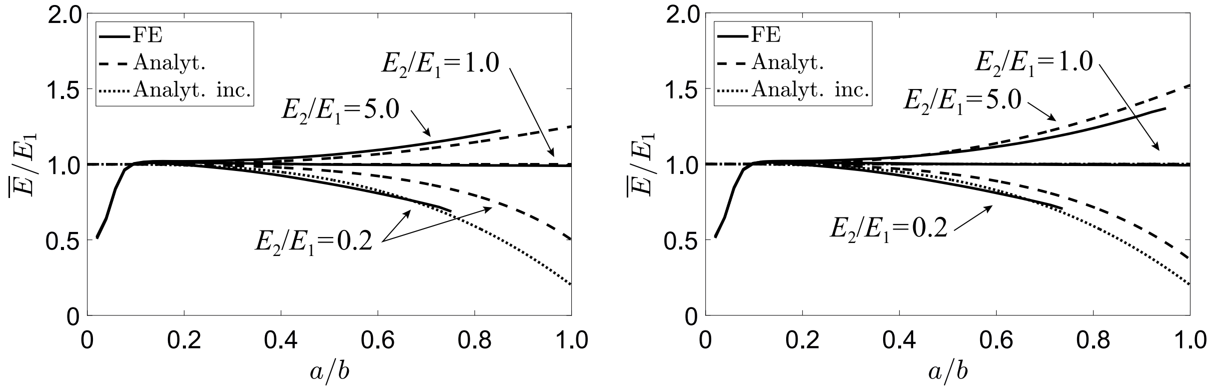

(c) $\nu_1 = \nu_2 = 0.2$ (d) $\nu_1 = \nu_2 = 0.3$

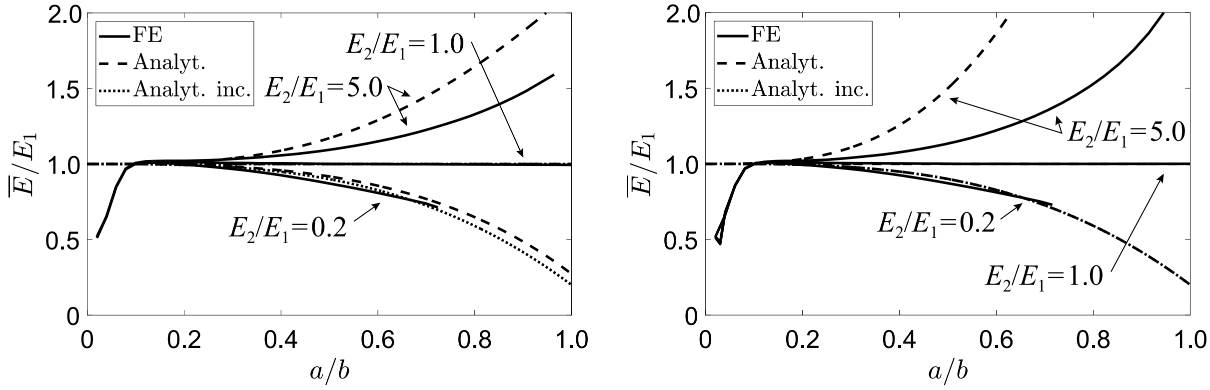

(e) $\nu_1 = \nu_2 = 0.4$ (f) $\nu_1 = \nu_2 = 0.5$

Figure 9: Indentation response of an elastic hemispherical particle embedded in an elastic half space. Dimensionless effective elastic modulus $\bar{E}/E_1$ versus dimensionless indentation radius a/b, as calculated by FE simulations and using Eq.(32) (black solid line), the analytical model Eq.(27) (black dashed line), and the analytical model for the incompressible material Eq.(31) (black dotted line). The results are shown for three values of modulus mismatch, $E_2/E_1 = 0.2$, 1.0, and 5.0, and for (a) $\nu_1 = \nu_2 = 0.0$, (b) $\nu_1 = \nu_2 = 0.1$, (c) $\nu_1 = \nu_2 = 0.2$, (d) $\nu_1 = \nu_2 = 0.3$, (e) $\nu_1 = \nu_2 = 0.4$, (f) $\nu_1 = \nu_2 = 0.5$.

ulus equals the Young's modulus of the hemispherical particle. Under continued indentation, the effective modulus of the stiff particle configuration, $E_2/E_1 = 0.2$, monotonically decreases, for the homogeneous material, $E_2/E_1 = 1.0$, it remains constant and equals $\bar{E} = E_1$, and for the compliant particle configuration, $E_2/E_1 = 5.0$, it monotonically increases. In agreement with the observation made from Figure 8, for the stiff particle configuration, $E_2/E_1 = 0.2$, the analytical model for the incompressible bi-material closely matches the effective modulus determined from the FE simulations. For the homogeneous material the general analytical expression, Eq.(27), and the expression for the incompressible bi-material, Eq.(31), lead to the same result $\bar{E} = E_1$, which match the FE results. For the ~~soft~~ compliant particle configuration, $E_2/E_1 = 5.0$, the agreement between the effective modulus expression, Eq.(27), and the FE results is adequate for Poisson ratios in the range $0.2 \leq \nu_i \leq 0.3$ where $i \in \{1, 2\}$, and is adequate up to an indentation of $a/b = 0.3$ to 0.4 for Poisson ratios falling outside this range.

From the above comparison with the FE results (and from similar comparisons with FE results for alternative stiffness mismatches $E_2/E_1 = 0.5$ and 2.0, but omitted here for the sake of brevity), it is concluded that the analytical expressions for the effective elastic modulus $\bar{E}$ of the indented bi-material given by Eqs.(27) and (31) are adequate for a broad range of stiffness mismatches, $0.2 \leq E_2/E_1 \leq 5.0$, and Poisson ratios, $0 \leq \nu_i \leq 0.5$ with $i \in \{1, 2\}$, within the following regimes of the normalized indentation radius a/b:

$$\bar{E} = \begin{cases} \dfrac{E_1(-E_2(a^3 + 2b^3 + (a^3 - 4b^3)\nu_1) + (a^3 - b^3)E_1(1 + \nu_2))(1 + \nu_1)}{(a^3 + 2b^3)E_2(2\nu_1^2 + \nu_1 - 1) - E_1(-a^3 + b^3 + (2a^3 + b^3)\nu_1)(1 + \nu_2)}\,, \\ \quad \text{for} \quad 0 \leq a/b \leq 1 \quad \text{if} \quad 1.0 < E_2/E_1 \leq 5.0 \quad \text{and} \quad 0.2 \leq \nu_i \leq 0.3\,, \\ \quad \text{for} \quad 0 \leq a/b \leq 0.3 \quad \text{if} \quad 1.0 < E_2/E_1 \leq 5.0 \quad \text{and} \quad 0 \leq \nu_i < 0.2 \quad \text{or} \quad 0.3 < \nu_i \leq 0.5\,, \\ \quad \text{for} \quad 0 \leq a/b \leq 1 \quad \text{if} \quad 0.5 < E_2/E_1 < 1.0 \quad \text{and} \quad 0.3 \leq \nu_i \leq 0.4\,, \\ \quad \text{for} \quad 0 \leq a/b \leq 0.5 \quad \text{if} \quad 0.5 < E_2/E_1 < 1.0 \quad \text{and} \quad 0 \leq \nu_i < 0.3 \quad \text{or} \quad 0.4 < \nu_i \leq 0.5\,, \\ \dfrac{E_1\left(b^3 - a^3\right) + E_2 a^3}{b^3}\,, \\ \quad \text{for} \quad 0 \leq a/b \leq 0.6 \quad \text{if} \quad 0.2 \leq E_2/E_1 \leq 0.5 \quad \text{and} \quad 0 \leq \nu_i \leq 0.5\,, \\ \quad \text{with} \quad i \in \{1, 2\}\,. \end{cases} \tag{33}$$

~~Note that~~ In the above expressions the various regimes follow each other through the specific ranges selected for the elastic parameters. The homogeneous limit $E_2/E_1 = 1$ is omitted from Eq.(33), but, as has already been mentioned, the ~~result is correctly~~ correct limit is obtained from this equation as $\bar{E} = E_1$ for the complete range of Poisson ratios $0 \leq \nu_i \leq 0.5$. Further, the maximum indentation radius $a/b = 1$ for simplicity has been included in the applicability

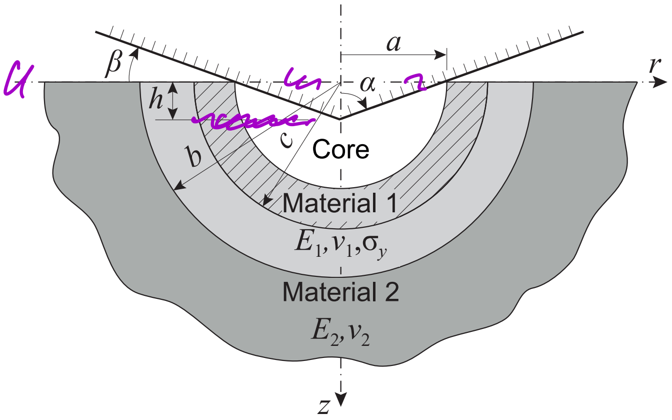

Figure 10: Indentation of an elastic, ideally plastic hemispherical particle of radius b (material 1) embedded in an elastic half space (material 2), by an indenter of semi-apex angle α. The indentation produces a hemispherical core of radius equal to the contact radius a, and a hemispherical plastic zone of radius c.

ranges of Eq.(33), although for certain combinations of elastic parameters the maximum value of a/b may be somewhat smaller than unity, due to the fact that the indenter prematurely touches the supporting material 2 under a relatively large vertical deformation of material 1, see also Figures 8 and 9.

4.2. Indentation of an elastic, ideally plastic hemispherical particle embedded in an elastic half space

The elastic configuration studied in Section 4.1 is now extended to the case of an elastic, ideally plastic hemispherical particle (material 1) embedded in an elastic half space (material 2), see Figure 10. The size of the plastic zone generated within the hemispherical particle is denoted by the radius c. The plastic zone can expand until it reaches the material interface between the hemispherical particle and the supporting elastic half space, $c = b$, or until the indenter reaches the material interface, $a = b$. The indentation response of the bi-material configuration is analysed analytically by an adapted version of Johnson's cavity expansion model for a homogeneous material Eq.(15), and numerically by means of finite element analyses. The adaptation of Johnson's model involves the replacement of the Young's modulus E in Eq.(15)

by the analytical expression for the effective elastic modulus $\bar{E}$ of the bi-material, leading to

$$\frac{p_m}{\sigma_y} = \begin{cases} \dfrac{p}{\sigma_y} + \dfrac{2}{3} \quad \text{for} \quad 2 \leq \dfrac{\bar{E}\tan\beta}{\sigma_y} \leq 27, \\ 2.8 \quad \text{for} \quad \dfrac{\bar{E}\tan\beta}{\sigma_y} > 27\,, \end{cases} \tag{34}$$

where

$$\frac{p}{\sigma_y} = \frac{2}{3}\left(1 + \ln\left(\frac{1}{3}\frac{\bar{E}\tan\beta}{\sigma_y}\right)\right)\,,$$

with $\bar{E}$ given by Eq.(27). Instead of Eq.(27), the refined, more complicated stiffness expression, Eq.(33), could have been used, but ~~it is expected that, due to the contribution of plasticity effects~~, this leads to only minor differences in the elasto-plastic indentation response.

Figure 11 illustrates the indentation response from both the FE simulations and the analytical cavity expansion model of the bi-material, Eq.(34). The Poisson ratios of the materials 1 and 2 are taken to be $\nu_1 = \nu_2 = 0.35$. Note that the incorporation of the effective elastic modulus $\bar{E}$ of the bi-material in the dimensionless parameter $(\bar{E}\tan\beta)/\sigma_y$ plotted along the horizontal axis is consistent with the analytical expression in Eq.(34). Consequently, the response plotted for the cavity expansion model includes the role of stiffness mismatch E_2/E_1. As already discussed in Section 2.3, the mean FE response for a homogeneous material, $\bar{E} = E_1 = E_2$, is adequately approximated by the cavity expansion model. The mean FE responses for the bi-material refer to a high stiffness ratio $E_2/E_1 = 10$ (red solid line) and to a low stiffness ratio $E_2/E_1 = 0.1$ (blue solid line). These FE responses are calculated by performing separate analyses for 9 different values of yield strength σ_y, which start along the horizontal axis at 9 ~~different~~ selected values of $(\bar{E}\tan\beta)/\sigma_y$. In correspondence with the range of validity of the cavity expansion model, the FE analyses are continued until the plastic zone reaches the material interface, $c = b$, or the indenter reaches the material interface, $a \approx b$.

For small indentations the contribution of the supporting material 2 to the overall response is negligible, as a result of which the effective modulus equals that of the hemispherical particle, $\bar{E} = E_1$. Under increasing indentation of the particle embedded in a relatively *compliant* half space, $E_2/E_1 = 0.1$, the values of $(\bar{E}\tan\beta)/\sigma_y$ and p_m/σ_y *decrease* in the initial elastic regime and also in the subsequent elasto-plastic regime. Specifically, the contribution of the compliant half space to the response grows with increasing indentation, so that the values of the mean hydrostatic stress $p_m = F/A_p$ and the effective modulus $\bar{E}$ diminish, as already observed for the elastic responses shown in Figures 8 and 9, respectively. For the same reason, the elastic and elasto-plastic indentation responses of the particle embedded in a relatively *stiff* half space, $E_2/E_1 = 10$, reveal an *increase* of $(\bar{E}\tan\beta)/\sigma_y$ and p_m/σ_y. Note further that, in the final, plastic regime, the mean indentation pressure p_m is almost insensitive to the elastic properties of the bi-material, and is essentially set by the yield strength σ_y.

In summary, the elastic, ideally plastic indentation response of a bi-material can be quantified in terms of the effective elastic modulus, Eq.(27), in the representation in Figure 11, with the FE results supporting the analytical cavity expansion model, Eq.(34). Thus, the cavity expansion model can be used as a practical, analytical tool to estimate the elasto-plastic material properties of embedded samples from indentation tests.

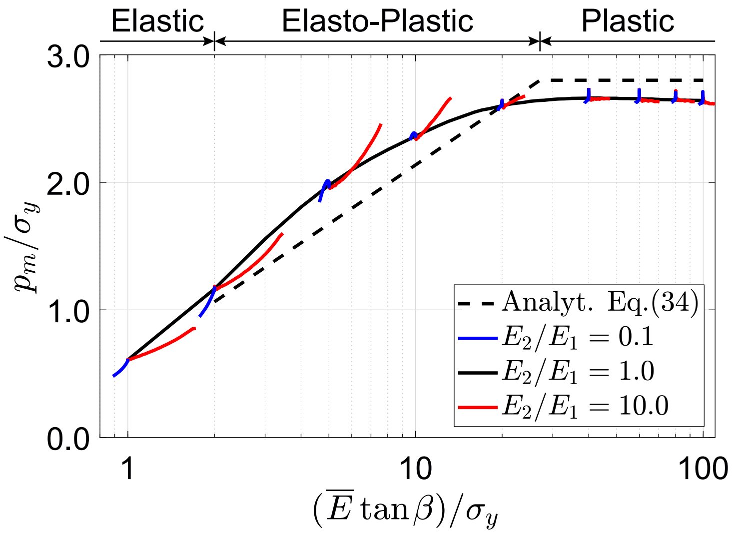

Figure 11: Indentation of an elastic, ideally plastic hemispherical particle embedded in an elastic half space. Mean indentation pressure p_m normalized by the yield strength σ_y as a function of the dimensionless parameter $(\bar{E}\tan\beta)/\sigma_y$, with $\bar{E}$ given by Eq.(27). The FE results are depicted for a homogeneous solid, $E_2/E_1 = 1$ (black solid line), and for bi-materials with modulus mismatches $E_2/E_1 = 0.1$ (blue solid line) and $E_2/E_1 = 10$ (red solid line), with 9 initial values of $(\bar{E}\tan\beta)/\sigma_y$. The Poisson's ratios are $\nu_1 = \nu_2 = 0.35$. The analytical result for the cavity expansion model of the bi-material Eq.(34) (black dashed line) holds for arbitrary value of the stiffness mismatch E_2/E_1 via the parameter $\bar{E}$.

5. Case Study: use ~~Applicability~~ of analytical model to interpret indentation test on embedded paint sample

The practical applicability of the analytical expression for the effective modulus, Eq.(27), is demonstrated through a case study on indentation tests taken from the literature [21]. ~~The~~ Indentation tests were performed on an acrylic, titanium white paint layer of Golden Artist

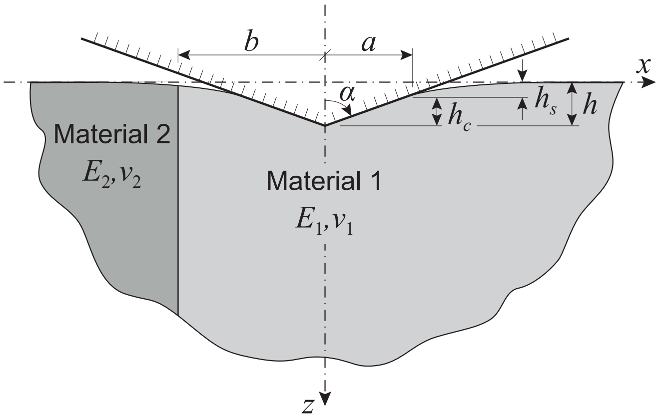

Figure 12: Indentation of a semi-infinite elastic bi-material with a straight, vertical material interface. The indentation of material 1 (paint) is performed at a distance b from the interface with material 2 (resin). The indentation depth h relates to a contact radius a, a contact depth h_c, and a sink-in depth h_s. The configuration is representative of the embedded paint sample tested in [21].

Colors® (material 1) that was fully embedded in a resin specified as a Technovit® 2000 LC fixing paste (material 2). The width of the paint sample was 210 µm and the thickness in the depth direction was considerably larger, above 1 mm. The reduced modulus measured by indenting the resin with a diamond Berkovich indenter was $E_r \approx 15$ GPa [21]. Assuming a representative value of $\nu_2 = 0.35$ for the Poisson's ratio of the resin, Eq.(3) implies that $E_2 \approx E_r(1-\nu_2^2) = 13.2$ GPa.

The challenge is to deduce the Youngs modulus of the paint from the measured unloading modulus S of an indentation test on the paint layer.

A sketch of the geometry at the material interface and the characteristics of the indenter is presented in Figure 12. The embedded paint sample was subjected to two indentations, performed at distances $b = 12$ µm and $b = 72$ µm from the vertical interface between the paint and the resin. The indentation tests were carried out using a continuous stiffness measurement (CSM) technique, entailing harmonic loading of amplitude F_0 at a frequency of 20 Hz, superimposed on the quasi-static loading. This allows for the determination of the contact stiffness as a function of indent depth without interrupting the indentation [6, 40]. The amplitude h_0 of the induced dynamic oscillation was on the order of nanometers, much less than that of the quasi-static signal. The unloading contact stiffness S ~~$=$~~ equals $(F_0/h_0)\cos\delta$, where δ is the phase shift between the harmonic load and displacement induced in the embedded viscoelastic paint sample [6, 58, 59, 60].

The contact stiffness S measured at a specific quasi-static loading step F_{max} and corresponding indentation depth h_{max} provides the actual contact depth h_c through Eq.(14) (using $\xi = 0.75$), which, under the assumption of a perfect Berkovich indenter, subsequently renders the contact area as $A_p = \pi a^2 = \pi(h_c \tan\alpha)^2$ [38], where $\alpha = 68.6°$ for the Berkovich indenter employed in the experiment [21]. From the value of A_p and the corresponding value of S, the effective modulus $\bar{E}$ of the bi-material is calculated as

$$\bar{E} = \frac{\sqrt{\pi}}{2} \frac{S(1-\nu_1^2)}{\gamma\sqrt{A_p}} \,. \tag{35}$$

Equation (35) is an approximation based on Eq.(9) for a homogeneous solid, whereby the Young's modulus E is replaced by the effective modulus $\bar{E}$. Further, the factor γ given by Eq.(30) has been added to correct for the artificial overlap between the indenter geometry and the deformed material surface, which typifies Sneddon's solution, Eq.(9). The accuracy of Eq.(35) for determining the effective modulus of the experimental bi-material configuration sketched in Figure 12 has been confirmed in Appendix A via a comparison with the indentation result obtained from a detailed, three-dimensional FE simulation. Since the Berkovich indenter used in the experiment generates a triangular shape indent, the effective modulus computed with Eq.(35) needs to be multiplied by a correction factor $1/\zeta$, with $\zeta = 1.034$, recall ~~see also~~ the discussion below Eq.(9).

Figures 13(a) and (b) show the normalized effective modulus, $\bar{E}/E_1$, as a function of the normalized contact radius a/b of the indenter, as measured at distances $b = 12$ µm and $b = 72$ µm from the material interface, respectively. The grey circles represent the experimental data in the format provided by the stiffness expression, Eq.(35), and the black solid line reflects the result from the analytical model, Eq.(27). In both figures the experimental data is accurately matched by the analytical model, whereby it is observed that the indentation response close

explain in a footnote that they sent the data for S(h) etc.

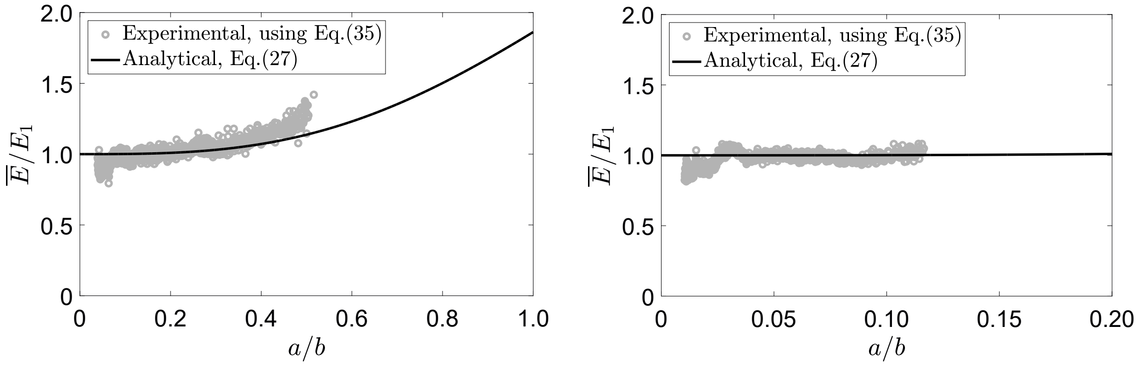

(a) $b = 12$ µm (b) $b = 72$ µm

Figure 13: Indentation response of a paint sample embedded in a resin. Dimensionless effective elastic modulus $\bar{E}/E_1$ versus the dimensionless indentation radius a/b, as determined from the experimental data in [21] via Eq.(35) (grey circles), and from the analytical model, Eq.(27) (black solid line). The indentations were performed at distances (a) $b = 12$ µm and (b) $b = 72$ µm from the material interface between the paint sample and the supporting resin, see Figure 12 for the geometrical characteristics at the material interface.

to the material interface, $b = 12$ µm, reveals a stiffening effect caused by the supporting resin. This stiffening effect increases monotonically with indentation depth, and remains absent if the indenter is sufficiently far away from the material interface, as can be clearly seen in Figure 13(b) for $b = 72$ µm. Upon ~~When~~ assuming the Poisson's ratio of the paint to be $\nu_1 = 0.35$ [52], together with the elastic parameters of the resin, $E_2 = 13.2$ GPa and $\nu_2 = 0.35$, the Young's modulus E_1 of the paint material is obtained from Figures 13(a) and (b) by evaluating the calibrated curves for the effective modulus $\bar{E}$ at $a/b = 0$, resulting in $E_1 = 1.8$ GPa for the indentation at $b = 12$ µm, and $E_1 = 1.4$ GPa, for the indentation at $b = 72$ µm. ~~Interestingly,~~ T these modulus values are in close correspondence with the values following from the calibration procedure applied in [21], whereby the indentation response was corrected by compensating for the overall structural compliance of the embedded paint sample. The relative difference of 22% in the above two modulus values is likely caused by spatial material heterogeneities in the test sample. With this result, the average stiffness mismatch of the embedded paint sample becomes $E_2/E_1 = 13.2/1.6 = 8.3$. Although this stiffness mismatch is somewhat higher than the initially estimated stiffness mismatch of $E_2/E_1 = 5.0$ adopted for generating the results of the comparison study depicted in Figure 14 in Appendix A, it may be reasonably expected that this does not significantly affect the accuracy of the calibration procedure.

Hide this in the Appendix!

6. Conclusions

An analytical model has been successfully developed to deduce the elastic and plastic properties of embedded samples from indentation measurements. The model makes use of the analytical expressions for the elastic and elasto-plastic indentation responses of homogeneous materials, but adapts them by the introduction of an effective modulus for the embedded sample. The range of validity of the predictions has been established by comparing the analytical results for various bi-material configurations with those from detailed finite element method simulations. The analyses show that, in the elastic and elasto-plastic regimes, the indentation response may be substantially influenced by the modulus of the embedding material. In the fully plastic regime the response is essentially set by the yield strength of the embedded particle. The practical applicability of the indentation model has been demonstrated by deducing the elastic modulus of a paint from indentation measurements on an embedded paint sample as reported in the literature.

Need to also state in text, otherwise, there is confusion where the data of Fig. 13 comes from.

Acknowledgments

The authors are grateful to Dr. Naoki Fujisawa and Dr. Michał Łukomski of The Getty Conservation Institute in Los Angeles, U.S.A. for the helpful digressions on their indentation experiments of embedded paint samples and for providing the raw experimental data. A.S.J.S. gratefully acknowledges the support of the European Union's Horizon 2020 research and innovation programme CollectionCare, under grant agreement N. 814624. E.B. is grateful for the support by the Netherlands Organization for Scientific Research (NWO), Project 15873, "Engineering goes Beauty - A computational multi-physics modelling approach towards the preservation of historical oil paintings", within the funding scheme "NWO Veni Award". N.A.F. is grateful for funding from the European Research Council (MULTILAT, grant number 669764).

Appendix A: Three-dimensional finite element model versus analytical model for a paint indentation problem

The bi-material configuration sketched in Figure 12 represents a paint (material 1) embedded in a resin (material 2), which has been subjected to indentation testing as reported in [21], see also Section 5. The suitability of the analytical model, Eq.(27), for determining the effective stiffness $\bar{E}$ of this configuration is assessed by means of a comparison with the results obtained from a detailed 3D FE indentation model. The 3D FE simulation is carried out in a similar fashion as described in Section 2.3 for the axisymmetric indentation models. For the tests performed in [21] the sample depth and width are considerably larger than the indentation contact radius a and the distance b between the indenter and the material interface; consequently, the geometry of the embedded sample is treated as semi-infinite. The origin of the (x, y, z) coordinate system shown in Figure 12 corresponds to the horizontal centre point of the half space configuration, and is located along the free upper boundary, at a distance b from the vertical interface between the paint (material 1) and the supporting resin (material 2). The dimensions of the FE geometry are $100 \times 100 \times 50$ μm^3. This tetragonal volume is discretized using 8-node iso-parametric brick elements with a $2 \times 2 \times 2$ Gauss quadrature. The model symmetry in the y-direction is exploited by applying appropriate fixed and roller supports along the $x - z$ plane that crosses the origin of the (x, y, z) coordinate system. The semi-infinite character of the half space is simulated by placing 8-node infinite elements along

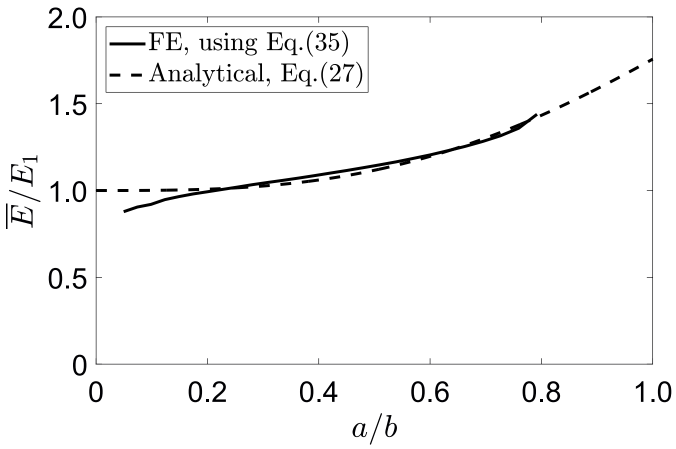

Figure 14: Indentation response of the semi-infinite elastic bi-material with a straight, vertical material interface as shown in Figure 12 (which represents an embedded paint sample). The modulus mismatch equals $E_2/E_1 = 5.0$ and the Poisson's ratios are $\nu_1 = \nu_2 = 0.35$. Dimensionless effective elastic modulus $\bar{E}/E_1$ versus the dimensionless indentation radius a/b, as determined from applying the stiffness expression Eq.(35) (solid line) to the FE results, and from the analytical model Eq.(27) (dashed line).

the lateral boundaries and the lower boundary of the FE model. The FE mesh is constructed by employing 606786 finite elements and 22594 infinite elements, whereby the mesh density is increased towards the indenter tip for obtaining highly accurate numerical results, as confirmed from a mesh refinement study.

Figure 14 shows the effective modulus calculated with the FE model and the analytical model, by plotting the dimensionless modulus $\bar{E}/E_1$ versus the dimensionless indentation radius a/b for a stiffness mismatch of $E_2/E_1 = 5.0$ and Poisson's ratios of $\nu_1 = \nu_2 = 0.35$. The value of the stiffness mismatch is considered as an initial estimate for the embedded paint sample tested in [21]. The effective modulus is deduced from the FE results by applying the stiffness expression Eq.(35), whereas for the analytical result it directly follows from Eq.(27). The unloading contact stiffness S in Eq.(35) is determined from the FE results via Eq.(13). ~~the discrete approximation of its definition given in Eq.(11), i.e., $S \approx \Delta F/\Delta h$, with ΔF and Δh the numerical increments of the applied load and the indentation depth, respectively.~~ The results of the FE simulation are plotted up to the stage at which the indenter reaches the supporting material 2; as indicated in Figure 12, the contact radius a is measured in the direction opposite to the material interface, so that the indenter reaches the material interface at a value a/b somewhat smaller than unity, i.e., $a/b = 0.76$. It can be observed in Figure 14 that the analytical effective modulus matches the numerical effective modulus closely over its full range of indentation radius a/b. Hence, the analytical model, Eq.(27), can be used for an accurate calibration of the experimental indentation response presented in [21] if the interpretation of the test data is done with the stiffness expression, Eq.(35).

References

[1] I. N. Sneddon, Boussinesq's problem for a rigid cone, Mathematical Proceedings of the Cambridge Philosofical Society 44 (4) (1948) 492–507.

[2] I. N. Sneddon, The relation between load and penetration in the axisymmetric Boussinesq problem for a punch of arbitrary profile, International Journal of Engineering Science 3 (1) (1965) 47–57.

[3] K. L. Johnson, The correlation of indentation experiments, Journal of the Mechanics and Physics of Solids 18 (2) (1970) 115–126.

[4] E. G. Herbert, G. M. Pharr, W. C. Oliver, B. N. Lucas, J. L. Hay, On the measurement of stress-strain curves by spherical indentation, Thin Solid Films 398-399 (2001) 331–335.

[5] J. H. Lee, Y. F. Gao, K. E. Johanns, G. M. Pharr, Cohesive interface simulations of indentation cracking as a fracture toughness measurement method for brittle materials, Acta Materialia 60 (15) (2012) 5448–5467.

[6] A. C. Fischer-Cripps, Nanoindentation, 3rd Edition, Springer, 2011.

[7] R. Saha, W. D. Nix, Effects of the substrate on the determination of thin film mechanical properties by nanoindentation, Acta Materialia 50 (1) (2002) 23 – 38.

[8] J. Hay, B. Crawford, Measuring substrate-independent modulus of thin films, Journal of Materials Research 26 (6) (2011) 727–738.

[9] K. Durst, M. Göken, H. Vehoff, Finite element study for nanoindentation measurements on two-phase materials, Journal of Materials Research 19 (1) (2004) 85–93.

[10] Y. T. Pei, G. M. Song, W. G. Sloof, J. Th. M. De Hosson, A methodology to determine anisotropy effects in non-cubic coatings, Surface and Coatings Technology 201 (16) (2007) 6911–6916.

[11] B. Vignesh, W. C. Oliver, G. Siva Kumar, P. Sudharshan Phani, Critical assessment of high speed nanoindentation mapping technique and data deconvolution on thermal barrier coatings, Materials & Design 181 (2019) 108084.

[12] T. E. Buchheit, T. J. Vogler, Measurement of ceramic powders using instrumented indentation and correlation with their dynamic response, Mechanics of Materials 42 (6) (2010) 599–614.

[13] J. Kimm, M. Sander, F. Pöhl, W. Theisen, Micromechanical characterization of hard phases by means of instrumented indentation and scratch testing, Materials Science and Engineering: A 768 (2019) 138480.

[14] N. A. Fleck, G. M. Muller, M. F. Ashby, J. W. Hutchinson, Strain gradient plasticity: theory and experiment, Acta Metallurgica et Materialia 42 (2) (1994) 475–487.

[15] W. D. Nix, H. Gau, Indentation size effects in crystalline materials: a law for strain gradient plasticity, Journal of the Mechanics and Physics of Solids 46 (3) (1998) 411–425.

[16] K. Durst, M. Göken, G. M. Pharr, Indentation size effect in spherical and pyramidal indentations, Journal of Physics D: Applied Physics 41 (7) (2008) 074005.

[17] G. M. Pharr, E. G. Herbert, Y. Gao, The indentation size effect: a critical examination of experimental observations and mechanistic interpretations, Annual Review of Materials Research 40 (2010) 271–292.

[18] M. R. Maughan, A. A. Leonard, D. D. Stauffer, D. F. Bahr, The effects of intrinsic properties and defect structures on the indentation size effect in metals, Philosophical Magazine 97 (20) (2017) 1902–1920.

[19] J. Salvant, E. Barthel, M. Menu, Nanoindentation and the micromechanics of Van Gogh oil paints, Applied Physics A: Materials Science & Processing 104 (2011) 509–515.

[20] A. Freeman, M. Łukomski, V. Beltran, Mechanical characterization of a cross-sectional TiO_2 acrylic-based paint by nano-indentation, Journal of the American Institute for Conservation 59 (1) (2020) 27–39.

[21] N. Fujisawa, M. Łukomski, Nanoindentation near the edge of a viscoelastic solid with a rough surface, Materials & Design 184 (2019) 108174.

[22] M. Tiennot, E. Paardekam, D. Iannuzzi, E. Hermens, Mapping the mechanical properties of paintings via nanoindentation: a new approach for cultural heritage studies, Scientific Reports 10 (2020) 7924.

[23] G. dePolo, M. Walton, K. Keune, K. R. Shull, After the paint has dried: a review of testing techniques for studying the mechanical properties of artists' paint, Heritage Science 9 (2021) 68.

[24] M. Łukomski, A. Bridarolli, N. Fujisawa, Nanoindentation of historic and artists' paints, Applied Sciences 12 (2022) 1018.

[25] W. Yan, C. L. Pun, Z. Wu, G. P. Simon, Some issues on nanoindentation method to measure the elastic modulus of particles in composites, Composites Part B: Engineering 42 (8) (2011) 2093–2097.

[26] F. Pöhl, S. Huth, W. Theisen, Finite element method-assisted acquisition of the matrix influence on the indentation results of an embedded hard phase, Materials Science and Engineering: A 559 (2013) 822–828.

[27] T. F. Low, C. L. Pun, W. Yan, Theoretical study on nanoindentation hardness measurement of a particle embedded in a matrix, Philosophical Magazine 95 (14) (2015) 1573–1586.

[28] X. Chen, J. J. Vlassak, Numerical study on the measurement of thin film mechanical properties by means of nanoindentation, Journal of Materials Research 16 (10) (2001) 2974–2982.

[29] J. E. Jakes, C. R. Frihart, J. F. Beecher, R. J. Moon, D. S. Stone, Experimental method to account for structural compliance in nanoindentation measurements, Journal of Materials Research 23 (4) (2008) 1113–1127.

[30] N. Fujisawa, T. F. Zhang, B. H. Lee, K. H. Kim, A robust method for extracting the mechanical properties of thin films with rough surfaces by nanoindentation, Journal of Materials Research 31 (23) (2016) 3777–3785.

[31] H. Y. Yu, S. C. Sanday, B. B. Rath, The effect of substrate on the elastic properties of films determined by the indentation test – axisymmetric Boussinesq problem, Journal of the Mechanics and Physics of Solids 38 (6) (1990) 745–764.

[32] H. Gao, C.-H. Chiu, J. Lee, Elastic contact versus indentation modeling of multi-layered materials, International Journal of Solids and Structures 29 (20) (1992) 2471–2492.

[33] I. I. Argatov, F. J. Sabina, Small-scale indentation of an elastic coated half-space: The effect of compliant substrate, International Journal of Engineering Science 104 (2016) 87–96.

[34] Y. Zhao, T. C. Ovaert, Error estimation of nanoindentation mechanical properties near a dissimilar interface via finite element analysis and analytical solution methods, Journal of Materials Research 25 (12) (2010) 2308–2316.

[35] I. I. Argatov, F. J. Sabina, Small-scale indentation of a hemispherical inhomogeneity in an elastic half-space, European Journal of Mechanics A/Solids 53 (2015) 151–162.

[36] R. Hill, B. Storåkers, A. B. Zdunek, A theoretical study of the Brinell hardness test, Proceedings of the Royal Society of London. Series A: Mathematical, Physical and Engineering Sciences 423 (1865) (1989) 301–330.

[37] N. Ogbonna, N. A. Fleck, A. C. F. Cocks, Transient creep analysis of ball indentation, International Journal of Mechanical Sciences 37 (11) (1995) 1179–1202.

[38] W. C. Oliver, G. M. Pharr, An improved technique for determining hardness and elastic modulus using load and displacement sensing indentation experiments, Journal of Materials Research 7 (6) (1992) 1564–1583.

[39] Y.-T. Cheng, C.-M. Cheng, Scaling, dimensional analysis, and indentation measurements, Materials Science and Engineering: R: Reports 44 (4) (2004) 91–149.

[40] W. C. Oliver, G. M. Pharr, Measurement of hardness and elastic modulus by instrumented indentation: Advances in understanding and refinements to methodology, Journal of Materials Research 19 (1) (2004) 3–20.

[41] M. Zhao, X. Chen, N. Ogasawara, A. C. Razvan, N. Chiba, D. Lee, Y. X. Gan, New sharp indentation method of measuring the elastic–plastic properties of compliant and soft materials using the substrate effect, Journal of Materials Research 21 (12) (2006) 3134–3151.

[42] G. M. Pharr, A. Bolshakov, Understanding nanoindentation unloading curves, Journal of Materials Research 17 (10) (2002) 2660–2671.

[43] J. W. Harding, I. N. Sneddon, The elastic stresses produced by the indentation of the plane surface of a semi-infinite elastic solid by a rigid punch, Mathematical Proceedings of the Cambridge Philosophical Society 41 (1) (1945) 16–26.

[44] M. F. Doerner, W. D. Nix, A method for interpreting the data from depth-sensing indentation instruments, Journal of Materials Research 1 (4) (1986) 601–609.

[45] R. B. King, Elastic analysis of some punch problems for a layered medium, International Journal of Solids and Structures 23 (12) (1987) 1657–1664.

[46] D. M. Marsh, Plastic flow in glass, Proceedings of the Royal Society of London. Series A: Mathematical, Physical and Engineering Sciences 249 (1378) (1964) 420–435.

[47] K. L. Johnson, Contact Mechanics, Cambridge University Press, 1985.

[48] R. Hill, The Mathematical Theory of Plasticity, Oxford University Press, 1950.

[49] V. Tvergaard, A. Needleman, Polymer indentation: Numerical analysis and comparison with a spherical cavity model, Journal of the Mechanics and Physics of Solids 59 (9) (2011) 1669–1684.

[50] V. Tvergaard, A. Needleman, Effect of viscoplastic material parameters on polymer indentation, Modelling and Simulation in Materials Science and Engineering 20 (6) (2012) 065002.

[51] O. C. Zienkiewicz, C. Emson, P. Bettess, A novel boundary infinite element, International Journal for Numerical Methods in Engineering 19 (3) (1983) 393–404.

[52] E. W. S. Hagan, M. N. Charalambides, C. R. T. Young, T. J. S. Learner, S. Hackney, Influence of the inorganic phase concentration and geometry on the viscoelastic properties of latex coatings through the glass-transition, Polymer 52 (7) (2011) 1662–1673.

[53] T. A. Laursen, J. C. Simo, A study of the mechanics of microindentation using finite elements, Journal of Materials Research 7 (3) (1992) 618–626.

[54] N. A. Fleck, H. Otoyo, A. Needleman, Indentation of porous solids, International Journal of Solids and Structures 29 (13) (1992) 1613–1636.

[55] S. D. Mesarovic, N. A. Fleck, Spherical indentation of elastic-plastic solids, Proceedings of the Royal Society of London. Series A: Mathematical, Physical and Engineering Sciences 455 (1987) (1999) 2707–2728.

[56] P. Chadwick, The quasi-static expansion of a spherical cavity in metals and ideal soils, The Quarterly Journal of Mechanics and Applied Mathematics 12 (1) (1959) 52–71.

[57] J. C. Hay, A. Bolshakov, G. M. Pharr, A critical examination of the fundamental relations used in the analysis of nanoindentation data, Journal of Materials Research 14 (6) (1999) 2296–2305.

[58] E. G. Herbert, W. C. Oliver, G. M. Pharr, Nanoindentation and the dynamic characterization of viscoelastic solids, Journal of Physics D: Applied Physics 41 (7) (2008) 074021.

[59] E. G. Herbert, W. C. Oliver, A. Lumsdaine, G. M. Pharr, Measuring the constitutive behavior of viscoelastic solids in the time and frequency domain using flat punch nanoindentation, Journal of Materials Research 24 (3) (2009) 626–637.

[60] B. N. Lucas, W. C. Oliver, J. E. Swindeman, The dynamics of frequency-specific, depth-sensing indentation testing, MRS Proceedings 522 (1998) 3–14.